# Designing Resonance Microwave Cavities to Optimize Plasma Generation

Ana Megía-Macías, Elena Barrios-Díaz, Jean-Louis Jauberteau, Isabelle Jauberteau, and Osvaldo Daniel Cortázar

***Abstract*— Methodology for designing the 2.45-GHz microwave (MW) coupling system to optimize the hydrogen plasma density in an electron cyclotron resonance (ECR) plasma reactor is presented. Two different plasma generator systems have been studied by experiments and 3-D simulations to find the criteria to reach an optimized design. The experimental work includes the detailed measurements and calculations of the electron energy distribution functions (EEDF) and ultrafast photography diagnostics to estimate the spatial distributions of plasma unbalanced charge density, potential, and electric field for both cases. It demonstrates that to simulate in 3-D, the distribution of the resonant stationary electric field along the entire MW driver system can be used to improve the design in order to reach higher plasma densities and temperatures.**

***Index Terms*— Microwave (MW) coupling, MW design optimization, MW plasma, MW plasma reactor, MW resonance, plasma design optimization.**

## I. Introduction

COUPLING is a critical issue for a wide range of microwave (MW) and radio-frequency plasma reactors from accelerator ion sources to industrial systems applied to semiconductor industry [1], [2]. The physics involved in the process of energy transference from the MW generator to the plasma has been discussed many times in the literature [3]–[6], and the effect of plasma formation on the electric field profile, the resonant frequency of entire system, and the coupling factor are the topics of discussion in the low density and temperature plasma community [7], [8]. Plasma density and temperature play a key role in reactor characterization because they strongly define the kind of application and its performance. For ion sources, the relationship of plasma density and temperature with the extracted ion beam current and emittance, respectively, is a good example [9].

Two different plasma chambers and coupler systems, preliminary and optimized, are presented herein in a comparative study. A previous work on this subject was published by the authors showing a first approach where 3-D simulations of stationary $E$-field distribution inside the MW system were described as a useful tool for designing in an article entitled "Influence of MW coupling design on plasma density at Test-Bench for Ion Sources Plasma Studies (TIPS)" [10]. Here, we present a deeper work including further research with electron energy distribution function (EEDF) measurements with Langmuir probes and estimations of electrical field distribution and plasma potential based on ultrafast photography. We establish a correlation between the original work and the previous 3-D electric field simulations concluding that the later is a useful tool for MW plasma sources design optimization. In order to compare the 3-D simulations previously published with the new results described in this article, we are reproducing, here, the key figures in [10] (see Figs. 1, 3, 4, and 6).

The impact of resonance cavity design on plasma density and temperature is demonstrated for the first time in this extensive study by two different experimental methods. These original data clearly show the importance of entire MW system electric field distribution 3-D simulations as an excellent approach to an optimized plasma reactor design.

The experiments were conducted on a plasma reactor test bench where modifications of its components are relatively simple to make. The reactor is an electron cyclotron resonance (ECR) plasma generator where the plasma is produced inside a cylindrical plasma chamber by exciting a gas with 2.45-GHz MWs while embedded in an ECR magnetic field. The MW energy is provided by a 2.45-GHz magnetron that can be operated both in continuous wave (CW) or pulsed mode. The reactor has been previously described in detail in [11]–[13].

Once the plasma is formed inside the system, the resonant frequency changes due to the plasma itself being an electrical conductor with permittivity and permeability different from 1. Some interesting works to get an estimation of that change in frequency considering homogeneous plasma and estimating its density have been published [3]. However, the calculations of the electric field with the presence of plasma in the system are still very difficult. The resonant characteristics of the systems are highly distorted when the plasma is ignited, and

Manuscript received September 6, 2019; revised November 11, 2019; accepted November 19, 2019. Date of publication December 5, 2019; date of current version June 9, 2020. This work was supported in part by the Spanish Ministry of Economy and Competitiveness under Grant FIS2016-77132-R and in part by the European Union's H2020 Research and Innovation Program under Grant 654002 (ENSAR2-MIDAS). The Associate Editor coordinating the review process was Christoph Baer. *(Corresponding author: Ana Megía-Macías.)*

A. Megía-Macías is with the Mechanics, Design and Industrial Organization Department, University of Deusto, 48007 Bilbao, Spain (e-mail: ana.megia@deusto.es).

E. Barrios-Díaz and O. D. Cortázar are with the Institute for Energy Research (INEI), University of Castilla-La Mancha, 13170 Ciudad Real, Spain.

J.-L. Jauberteau and I. Jauberteau are with the IRCER, UMR 6638 CNRS, Faculté des Sciences et Techniques, Université de Limoges, 8060 Limoges, France.

Color versions of one or more of the figures in this article are available online at http://ieeexplore.ieee.org.

Digital Object Identifier 10.1109/TIM.2019.2957891

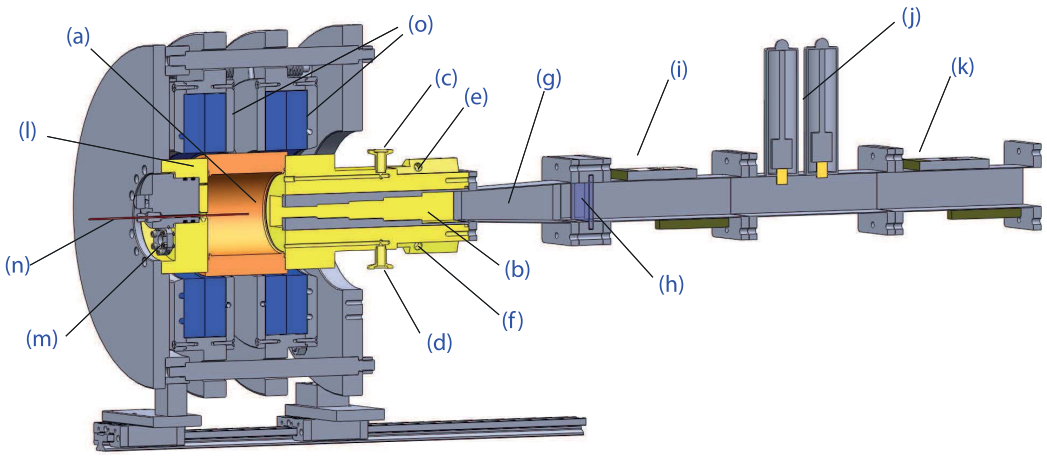


Fig. 1. Cross section of the plasma reactor with the preliminary design. (a) Plasma chamber, (b) MW coupler, (c) gas inlet, (d) pressure gauge flange, (e) cooling water inlet, (f) cooling water outlet, (g) waveguide WR284/WR300 transition, (h) vacuum window, (i) and (k) bidirectional couplers, (j) two-stub tuner, (l) diagnostics port, (m) observation window, (n) Langmuir probe, and (o) magnetic field generation system [10].

as plasmas are complex systems, they are very difficult to be taken into account in a simulation. Our first approach was to study the resonance of the system in a vacuum, i.e., just before the plasma ignition, and redesign the system to maximize the electric field in the center of the plasma chamber. COMSOL 4.2 [14] was used to obtain the electric field distribution along the whole system (plasma chamber, coupler, and MW guide) while exciting the lower transverse electric resonant mode ($TE_{111}$).

## II. Preliminary Design Description and Behavior

The preliminary design of the plasma chamber and the MW coupler system (hereinafter preliminary design) was made by the engineering supplier company Elytt Energy for the denominated BLISI ion source still under operation at ESS Bilbao [15]. A cross section of the device can be seen in Fig. 1. The plasma chamber marked with letter (a) is made of oxygen-free high thermal conductivity (OFHC) copper. Letter (b) refers to the MW coupler designed for the purpose of adapting the impedances between the standard waveguide WR284 and the chamber, and it has five ridged steps for this purpose. Fig. 1 also shows two vacuum ports, one for the gas injection (c) and one for the measurement of the gas pressure inside the plasma chamber (d). The whole system is refrigerated by a cool water closed circuit, and the input and output ports are marked with letters (e) and (f). A transition waveguide (g) is necessary to match the WR284 flange at the entrance of the coupler to the standard WR340 waveguide size. After this transition piece, a 10-mm vacuum break window isolates the area under vacuum from the atmospheric one (h). A bidirectional coupler (i) is used for the recording of synchronization signals, and a two-stub tuner (j) allows us to have a fine impedance tuning. A second bidirectional coupler (k) records the incoming and reflected power signals. On the opposite side of the plasma chamber, a diagnostic port (l) serves us for three different tasks: the connection of the pumping system, the allocation of a view port (m), and the installation of the Langmuir probe system (n). At both sides of the chamber, there are 2-mm-thick boron nitride disks. Four coils (o) around the plasma chamber generate the magnetic field required to ignite the plasma, and they are located in two structures (usually referred to as pancakes) that can be moved axially. There are two different ways to modify the magnetic field profile: the axial movement of the pancakes and the modulation of the current of each coil.

The methodology used for the preliminary design development followed the engineering criterion of impedance matching between parts. This MW system was conceived as a set of different coupled parts being the plasma chamber the most important one and, in consequence, the first one to be designed. Its dimensions were chosen in order for its $TE_{111}$ mode resonant frequency to be 2.45 GHz, and the MW coupler was designed to adapt the impedances between the chamber and the WR284 MW guide. Such a criterion is frequently used as a principle of design in many MW excitation systems [16]. However, once the system was experimentally tested, it showed an anomalous behavior with a strong tendency to allocate the plasma outside the discharge chamber, specifically in the MW coupler.

Our first approach to the problem was to associate the tendency of plasma formation inside the coupler with relative high pressure (HP) due to the fact that rear volume [near the end of the coupler (e)] is the most distant area from the pumping system. A small auxiliary quartz view port was placed in the holder of the 10-mm vacuum window (h) to place a photodiode with fiber optics in order to detect the presence of plasma outside the discharge chamber. Moreover, a pressure sensor was also placed in the window holder (h), and the pressure was indeed higher in this point than in other parts of the system but its value was not high enough to be the reason of plasma formation at this point.

After an extensive study of the working range, we determined a narrow set of experimental conditions that could correct this effect: low gas pressure inside the plasma chamber, magnetron power below 1500 W, and magnetic field profile

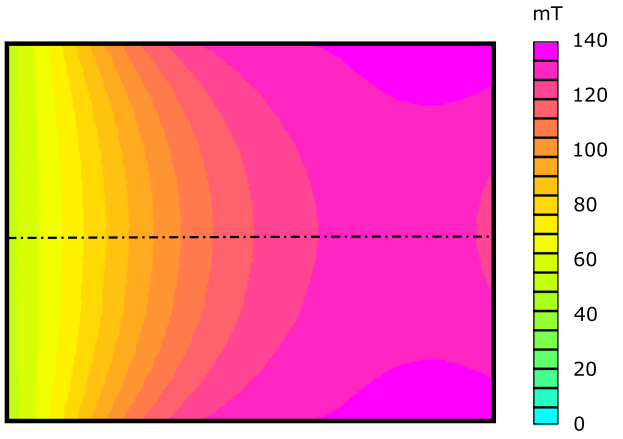


Fig. 2. Map of the magnetic field required to avoid the formation of plasma outside the plasma chamber when using the preliminary design.

more intense on the diagnostic port side than in the MW injection one. The latter is the most impacting factor. In order to correct this tendency, coils had to be moved along the $z$-axis to the extreme position close to the diagnostic port (extraction port in the ion source version BLISI), and the currents in each coil were properly tuned in a short range of values. Therefore, the external magnetic field configuration was practically fixed to obtain plasma formation inside the plasma chamber.

During the experiments, it was observed that relatively small changes in the magnetic field intensity or distribution could produce the alternating ignition of the plasma between the plasma chamber and the MW coupler. To allocate the plasma inside the discharge chamber only by incrementing the magnetic field intensity becomes unreachable. Fig. 2 shows a magnetic field 2-D plot in the longitudinal plane of the plasma chamber. This field was calculated using Finite Element Method Magnetics (FEMM) [17]. The external black frame represents the chamber contour MWs entering it from the right side and being the diagnostic port placed on the left. The results of the simulations were compared with the Hall probe experimental measurements, and the error was determined to be below 2%.

While looking for an explanation for such an undesirable behavior, some 3-D simulations of stationary electric field for the preliminary design were made. A typical result is shown in Fig. 3. Note that the maximum electric field value is allocated outside the plasma chamber, specifically inside the coupler piece where plasma showed a strong tendency to be established. This result motivated the development of an optimized design by changing the point of views and using the 3-D stationary electric field simulations tool, as is described in Section III.

## III. Optimized Design Description and Behavior

Fig. 4 shows a cross section of TIPS with the optimized design: chamber (a) and the MW coupler (b). The chamber was designed with a surrounding water cooling bath (c) inside its lateral wall. In order to be able to make easy modifications of the internal geometry of the MW coupler, two exchangeable inserts were designed (d). Letters (e) and (d) show the channels for pressure gauge connection and gas inlet.

The criterion used for developing the optimized design is opposite to the one described in Section II. It is based on the following concept: "if a resonant cavity is tightly coupled to some other MW circuits, the impact of physical modifications and the change in internal field distributions are so great that it can no longer be called the same cavity. In this case, the concept of an intrinsic resonant frequency of the cavity becomes meaningless, and we can only talk about the resonant frequency of the system as a whole" [18]. In order to facilitate the understanding of this methodology in practice, we follow by resuming the design steps, as they were previously published in [10].

As the first step and keeping in mind the previously described concept, we started by designing an isolated ideal cylindrical plasma chamber. Equation (1) [19] determines the resonant frequency of any TE mode in a cylindrical cavity as a function of its dimensions

$$f_{nml}^{TE} = \frac{c}{2\pi\sqrt{\mu_r \varepsilon_r}} \sqrt{\left(\frac{p'_{nm}}{a}\right)^2 + \left(\frac{l\pi}{d}\right)^2} \tag{1}$$

where $c$ is the speed of light, $\varepsilon_r$ is the relative electrical permittivity, $\mu_r$ is the relative magnetic permittivity inside the cavity (in our case, the medium inside the cavity is vacuum; therefore, $\varepsilon_r = \mu_r = 1$ ), $a$ is the radius of the cavity, $d$ is its length, $p_{nm}$ is the zero of order $m$ of the Bessel function of order $n$, and $p'_{nm}$ is its first derivative. The indexes $n$, $m$, and $l$ identify the TE mode electromagnetic field pattern. Using (1) and taking into account that the coils limit the size of the plasma chamber, the new chamber dimensions were chosen to in order to have its $TE_{111}$ mode at the magnetron frequency (2.45 GHz): 85-mm diameter and 113-mm length.

For the second step, the use of a 3-D electric stationary field simulation tool is required. Attaching any coupling part to the cavity implies a certain modification of the electric field inside. This has two main implications: resonant frequency of the whole system must be assumed to be, in general, different from the one of the cavities without the coupler, and the loses are higher. It is recommendable to simulate the entire ensemble conformed by the chamber directly connected to the waveguide to check such an effect despite the fact that it may not be possible to do it in practice due to practical reasons as in our case. The new resonant frequency obtained by 3-D simulation under such conditions was 2.42 GHz. These results highlight the need for a coupler to connect the waveguide and the plasma chamber. The coupler has different functions: on one hand, it serves to mechanically connect the waveguide and the plasma chamber; on the other hand, it must put the resonance frequency of all the system back to 2.45 GHz, and at the same time, it must maximize the intensity of the electric field inside the chamber while keeping it as low as possible outside it. Therefore, the logical third step is to introduce the coupler piece in simulations to reach both goals. In our case, a $\lambda/4$ length one-step ridged coupler gave the best simulations results. Simulations of the $E$-field resonance for both the preliminary and optimized results were previously published by Megía-Macías *et al.* [10]. Fig. 5 shows the final result

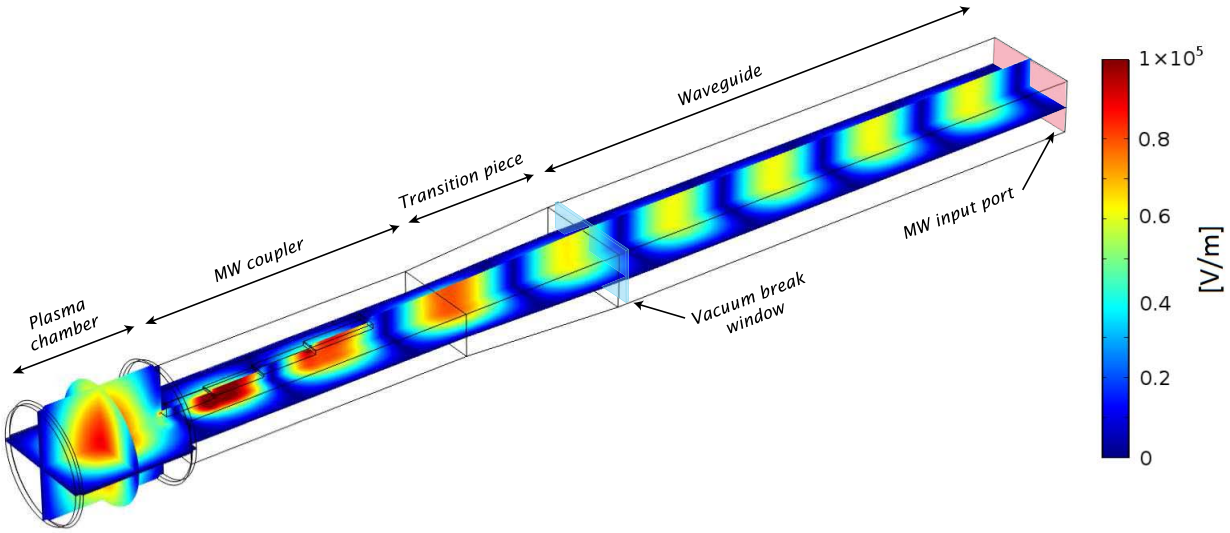


Fig. 3. Simulation of the $E$-field profile with the preliminary design. Input power 1500 W (continuous) at 2.45-GHz $TE_{10}$ port [10].

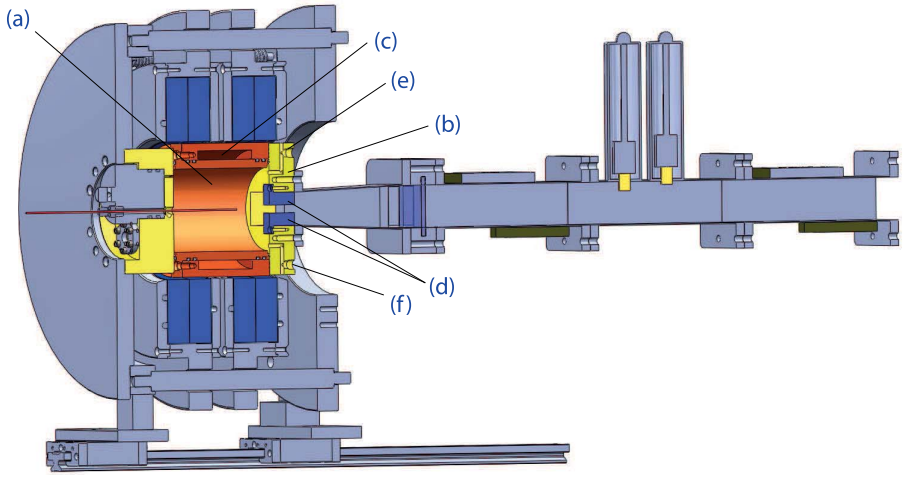


Fig. 4. Cross section of the reactor with optimized design. (a) Plasma chamber, (b) one-step ridged coupler, (c) water cooling chamber, (d) ridged exchangeable steps, (e) gas inlet, and (f) vacuum gauge connection channel [10].

of 3-D stationary electric field simulation for the optimized design once the final shape coupler piece has been reached. The contrast with Fig. 3 is remarkable.

## IV. Experimental Results and Comparison Between Designs

We started the experiments with the optimized design by trying to apply the same magnetic field distribution that was used before with the preliminary design, but this was not possible. The produced plasma was very unstable with high jitter during breakdown. Even though we intended to study both designs under the same experimental conditions, this tendency could only be prevented by changing the magnetic field distribution. Fig. 6 shows the new $B$-field profile used for the experiments with the optimized design. Once the magnetic field was changed, the plasma showed a stable robust behavior with respect to the $B$-field modifications (the changes in the position of the coils or in the current circulating through each of them). The ignition of the plasma outside the chamber completely disappeared, and we discovered a wider range of magnetic field configurations, gas pressures, and MW powers where the plasma could be stable with several spatial distribution modes [20]. This was very contrasting with the preliminary design system where the working range was very narrow, as previously described. In order to reach a better understanding of differences between both designs, we started a comparative study by measuring EEDFs and estimating plasma density distributions. The first was done by means of Langmuir's probes and the second by the implementation of ultrafast photography diagnostics.

### A. Measurements of EEDFs

Measurements have been performed by means of Langmuir's probes, and the EEDF has been resolved in space and time within each design.

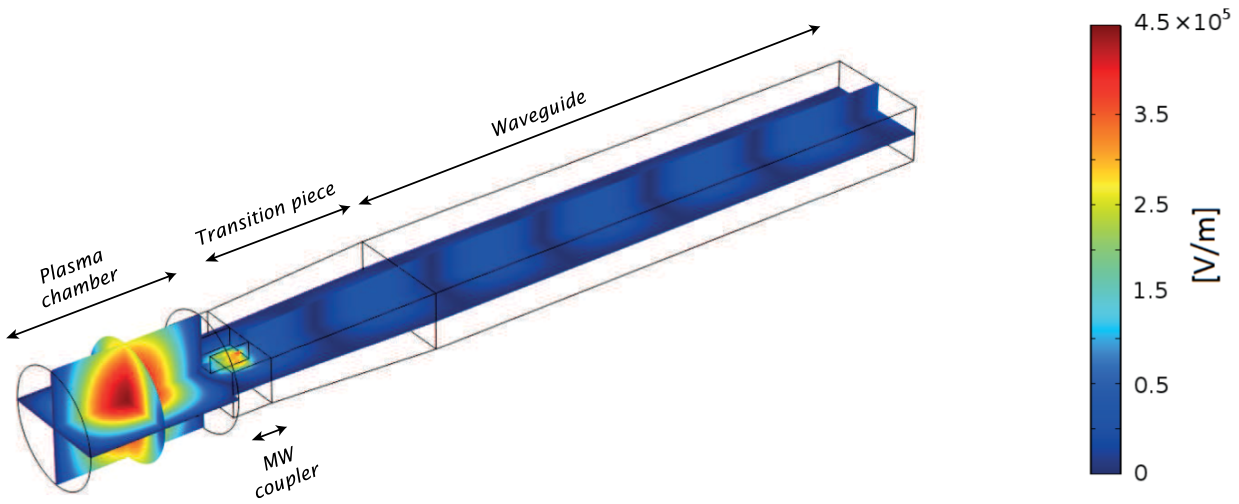


Fig. 5. Simulation of the $E$-field profile with the optimized design. Input power 1500 W (continuous) at 2.45-GHz $TE_{10}$ port [10].

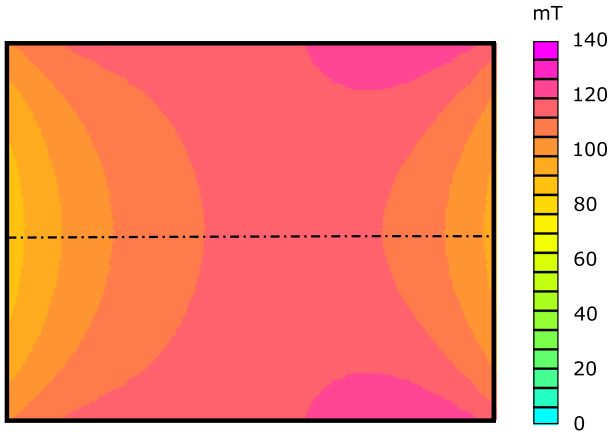


Fig. 6. Magnetic field map used for experiments with the optimized design.

*1) Method Used to Determine EEDFs:* Theoretical developments to correct perturbations in the plasma occasioned by the presence of the probe and the consequences on its characteristics curves were developed in the early 1960s by Shift [21]. It is possible to neglect such a disturbance if the electron diffusion rate is high enough to compete with electron draining from plasma to probe, but, unfortunately, this is not the case in our experiments, where such a correction is essential because EEDFs are different around the vicinity of the probe with respect to the farthest undisturbed plasma, as we explain as follows. In the case of a magnetoplasma, the electron diffusion coefficient is anisotropic because of the influence of magnetic field on the radial component of electron velocity. Due to electron gyration, radial (perpendicular to the magnetic field) and longitudinal (parallel to the magnetic field), electron diffusion coefficients are unequal; therefore, the disturbance of the probe cannot be neglected for high magnetic field intensity. The extension of Swift's theory for magnetoplasmas was developed by Arslenbekov *et al.* [22], Demidov *et al.* [23], and Popov *et al.* [24]. We just recall the main method lines for experimental data treatment summing up our recent works [25], [26] to facilitate the readability as follows.

In the case of a diffusion regime, the electron current depends on the diffusion parameters given by

$$I_e(U) = \frac{8\pi eS}{3m^2\gamma}\int_{eU}^{\infty}\frac{(\varepsilon_e - eU)f_0(\varepsilon_e)d\varepsilon_e}{1+((\varepsilon_e - eU)/\varepsilon_e)\Psi} \tag{2}$$

where $\varepsilon_e$ is the total electron energy in the sheath, $U$ is the probe potential with respect to the plasma potential, $\Psi(\varepsilon_e)$ is the diffusion parameter depending on $\varepsilon_e$, $S$ is the collecting probe area, $\gamma$ is a geometrical factor, and $f_0(\varepsilon_e)$ is the isotropic distribution function. It is correlated with the electron energy probability function $f(\varepsilon_e)$ given by

$$f(\varepsilon_e) = 4\pi\sqrt{2}\, m_e{}^{-3/2} f_0(\varepsilon_e) \tag{3}$$

and with the EEDF $F(\varepsilon_e)$ given by

$$\int_{\varepsilon e0}^{\infty} F(\varepsilon_e)d\varepsilon_e = \int_{\varepsilon e0}^{\infty} f(\varepsilon_e)\sqrt{\varepsilon_e}d\varepsilon_e = 4\pi\int_0^{\infty} v^2 f_0(v)dv = n_e \tag{4}$$

where $v$ and $n_e$ are the electron velocity and density, respectively. In (2), the diffusion parameter depends on the probe geometry and on the Larmor radius. In our case, the cylindrical probe was located at the center of the plasma chamber for both designs, and it is parallel to the magnetic field. Diffusion parameter is given by

$$\Psi = \frac{\pi L}{4\gamma\rho_e}. \tag{5}$$

The $\gamma$ factor can be approximated using $\gamma = 0.71 + (0.25/x)$, where $x$ is the ratio between the probe radius and Larmor radius [22]. By using (2), it can be shown that the second derivative of collected electron current by the probe is given by [22]

$$I''(U) = Cf(eU) - C\int_{eU}^{\infty} K(\varepsilon_e, U)f(\varepsilon_e)d\varepsilon_e \tag{6}$$

where $C$ is a constant, $C = e^3S/2\gamma\sqrt{2\,m_e}$, $S$ is the probe collector area, and the other coefficients have the

usual meaning

$$K(\varepsilon_e, U) = \frac{2\Psi {\varepsilon_e}^2}{[\varepsilon_e(1+\Psi) - \Psi eU]^3}. \quad (7)$$

It can be seen that without magnetic field, $B = 0$, $\Psi = 0$, and (6) becomes the Druyvesteyn equation.

*Resuming:* we calculate the EEDF by the second derivative of electron current assuming Druyvesteyn equation

$$f(\varepsilon) = \frac{2\sqrt{2m_e}}{e^3 S} I''(U). \quad (8)$$

and then, we determine the distribution function by successive adjustments of (6). Finally, the exact distribution function is obtained when the experimental values of the second derivative $I''(U)$ are equal to the calculated one by using (6), all over the entire electron energy range of the EEDF.

*2) EEDFs Measurements of Both Designs:* EEDFs have been measured in the optimized design for different experimental conditions, and the results are compared with the obtained for the preliminary design.

On one hand, it can be seen in our previous works [26], [27] that polymodal EEDFs are measured for the preliminary design during the discharge breakdown and decay for the pressure ranging from 0.38 to 0.62 Pa. The EEDF shape changes drastically from a nonresonant plasma ($B = 0.12$ T) to a resonant ECR plasma ($B = 0.087$ T) where the lowest EEDF profile was obtained at low pressure (LP) under OFF-resonance conditions, while the highest EEDF was obtained at LP under resonance conditions. It must be noticed that at LP and OFF-resonance conditions, the EEDF is strongly disturbed and the probe signal is very low compared with other experimental situations.

Three main components are generally observed in EEDFs measured in the preliminary design for three relative intensity settings [26], [27]: a low-energy component, observed at $\epsilon_e < 10$ eV, which increases with pressure, i.e., by increasing electron-neutral collision frequency; an intermediate component at energy ranges between 5 and 15 eV, which appears mainly in the ECR condition, when the input power is greater than 600 W, is the main component at 1500 W, and vanishes at OFF-resonance conditions with $B = 0.12$ T; and, finally, some small and broad components corresponding to the Maxwell–Boltzmann distribution ($T_e = 19$ eV) related to the electrons, which have not yet lost their inelastic energy while colliding with heavy particles, excited by the MW. This component is weaker than the other two, and it is more frequently observed when working under off-reference conditions.

It is worth noting that the polymodal shape of EEDFs is also observed in the optimized design. Fig. 7 shows a typical EEDF measured in the optimized design. It is formed by several components: the low-energy component (A) centered at 5.84 eV, corresponding to electrons suffering inelastic collision within the plasma and an intermediate component (B), observed at 20 eV, which was at about 13 eV in the preliminary design. The remaining EEDF tail is composed of two components, one at 14 eV (C1) and the other at 39 eV (C2). Due to the increase of the electron energy, the intermediate and high-energy components are observed at larger energy.

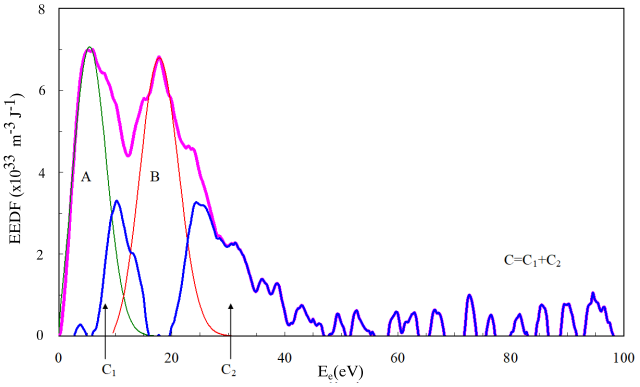


Fig. 7. Optimized design EEDF decomposition in different components: A, B, C1, and C2 with mean electron energies equal to 5.84, 19.97, 14.07, and 38.86 eV, respectively.

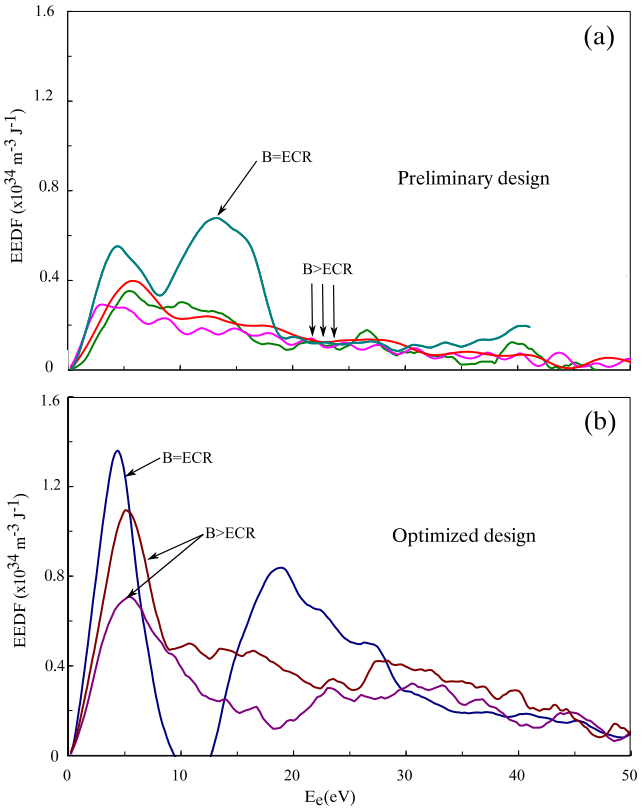


Fig. 8. Comparison of EEDF measured in (a) preliminary and (b) optimized designs at $2 \times 10^{-3}$ mBar, 1500 W with B = ECR and B > ECR.

The low-energy component, corresponding to electrons after collision with neutrals, still observed centered at the same energy.

A comparison between EEDFs in the preliminary and optimized designs for ECR and off-ECR conditions is shown in Fig. 8. Measurements are performed at 1500 W of incoming MW power and a pressure of $2 \times 10^{-3}$ mBar. Fig. 8(a) shows the EEDFs corresponding to the preliminary design and Fig. 8(b) to the optimized one. For B > ECR, the EEDF of the optimized design exhibits a high-energy component centered at about 30 eV, which is not observed in the preliminary design. For B = ECR, power absorption by electron due to ECR heating mechanism plays a more efficient role at the

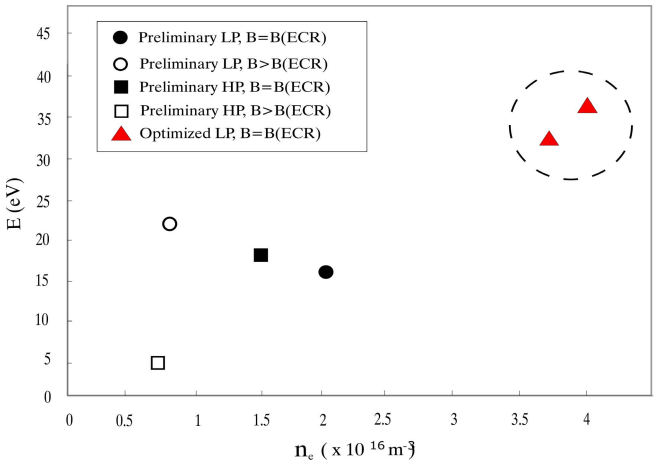


Fig. 9. Electron density versus electron energy. Comparison between measurements performed on the preliminary design at LP $1.6 \times 10^{-3}$ mBar and HP $2.6 \times 10^{-3}$ mBar with $B >$ ECR or $B =$ ECR and the optimized design at $2 \times 10^{-3}$ mBar at 1500 W of MW incoming power. The dashed circle highlights the values obtained in the optimized design.

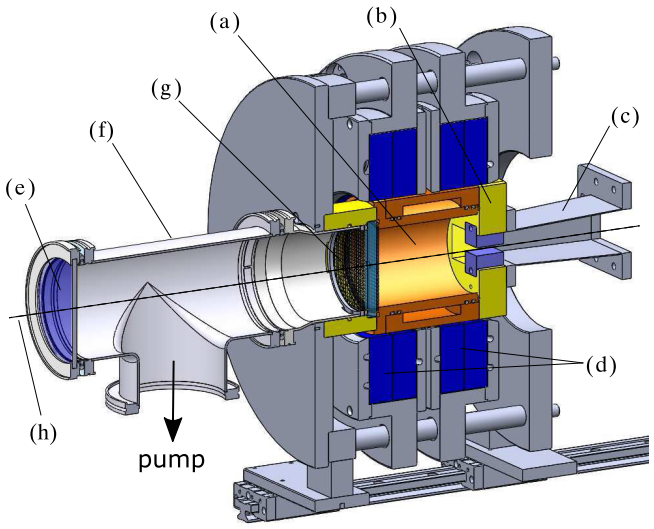


Fig. 10. Ultrafast pictures experimental arrangement: section view of the optimized design reactor. (a) Plasma chamber, (b) MW coupler, (c) tapered waveguide WR284/WR300 transition, (d) solenoids, (e) observation window, (f) vacuum tee, (g) transparent MW shielded window, and (h) ultrafast camera optical axis [30].

optimized design. The high-energy component is remarkable, and it corresponds to a larger mean value in the optimized design.

The measurements on the optimized design produce results where electron density and mean energy increase with respect to the preliminary design. If we compare electron density and mean electron energy measured in the optimized device with values from the preliminary one, a strong increment about 100% for electron density and 65% for mean electron energy is observed, as it can be seen in Fig. 9 where such values are highlighted inside a dashed circle.

### *B. Ultrafast Photography Diagnostics and Plasma Density Estimation*

The ultrafast photography diagnostics setup allows to obtain very high time-resolved picture sequences to study temporal evolutions of plasma spatial distributions [20], [28]–[32]. It uses a transparent plasma electrode consisting on a quartz window placed between two tungsten meshes that behaves as a metallic window from the MWs point of view but allows the observation of the plasma chamber interior and, as a consequence, the study of the different spatial distributions acquired by the plasma. Such an issue is essential because it keeps resonance characteristics of the entire MW system allowing to make comparisons with the previously obtained results where a full metal wall was used for Langmuir probe diagnostics as in our case. Fig. 10 shows a cross-sectional view of the plasma reactor with this setup installed. An ultrahigh-speed light intensified frame charge-coupled device (CCD) camera system was aligned on the optical axis (h) at 1 m of distance from the observation window (e) to take up to four image sequences in which delays between pictures and exposure times can be adjusted independently.

Typical exposure time was set at 1 $\mu$s as a usual good compromise between emitted light intensity and evolution plasma motion, while the delays between different photographs were set to follow the evolution of the plasma during the breakdown on each case. In our case, the delay has been fixed at the middle of pulse in order to get the plasma distribution once the steady stage has been reached. The gains in multichannel plates (MCPs) and CCDs were set in order to get the best definition possible in the pictures while avoiding saturation. The original black and white images are treated using a color scale, where red represents the maximum light intensity, while blue corresponds with the lower one. By using the obtained images, it is possible to make an estimation of the positive unbalanced plasma charge density spatial distributions, plasma potential, and electrical self-induced field [29], [32].

We start by assuming that the difference in mobility between the electrons and ions inside the plasma produces an unbalance in the charge distribution ($e\ (n_i - n_e) \geq 0$). This difference in electric charge between the different points of the plasma distribution generates an electrostatic potential $\phi$ in order to decrease the electron loss rate from the bulk of the plasma to the chamber wall. According to Poisson's equation

$$\varepsilon_0 \nabla^2 \phi = -e\ (n_i - n_e). \tag{9}$$

It is known that if the plasma can be considered to be optically thin, it is possible to assume that the emitted light intensity is proportional point-to-point to the ion density [33], [34], and the spatial distribution of the emitted light can then be used as a map for the unbalance on the electric charge distribution. Following this idea, we used the images of the plasma as a map of the positive free charge density distribution to solve (9). The mean plasma potential $V_p$ obtained by the Langmuir's probe diagnostics as described in Section IV-A was later used for the calibration of the electric charge value.

Here, we are using 2-D images that are the projection of the 3-D plasma structure; this is a limitation. However, we consider that it is a good approach to get a qualitative

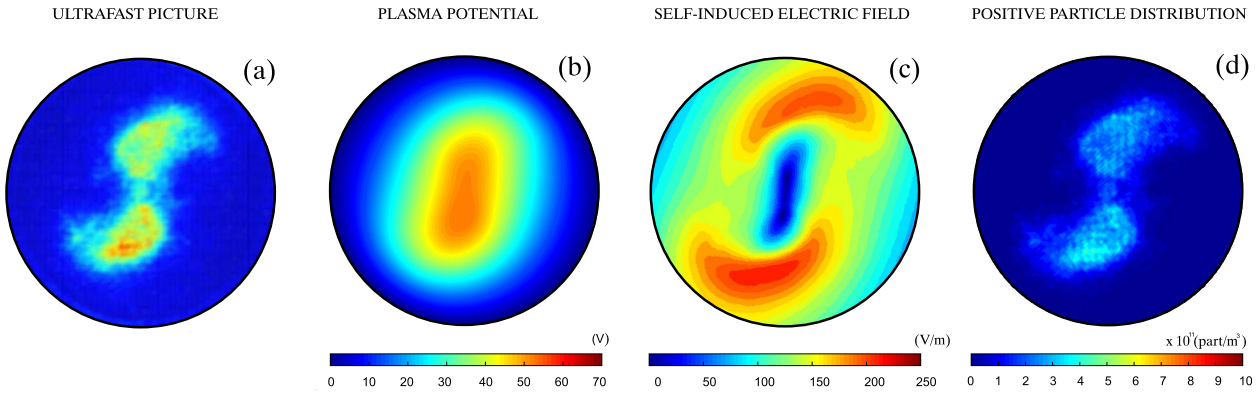


Fig. 11. Preliminary design sequence of 2-D calculations results starting from (a) typical ultrafast picture, followed by (b) calculated plasma potential, (c) self-induced electric field, and (d) positive particles distribution ($\times 10^{11}$ $part/\mathrm{m}^3$).

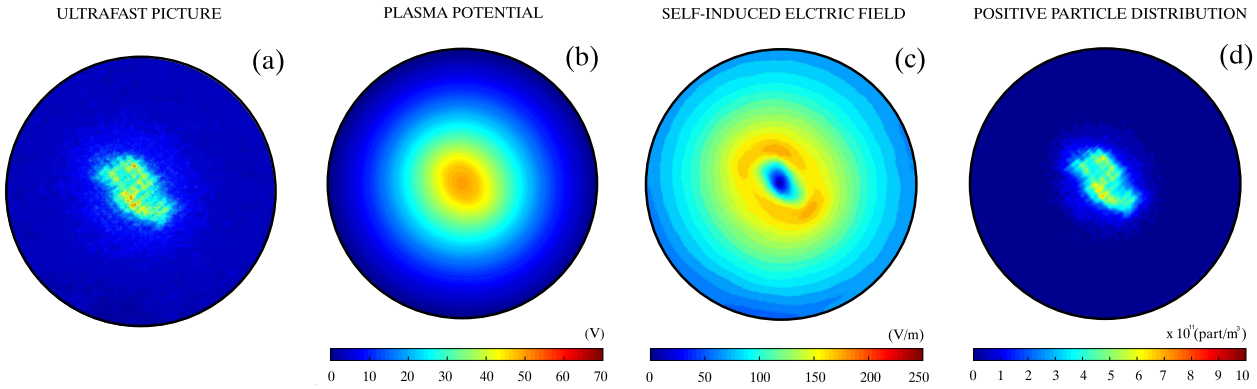


Fig. 12. Optimized design sequence of 2-D calculations results starting from (a) typical ultrafast picture, followed by (b) calculated plasma potential, (c) self-induced electric field, and (d) positive particles distribution ($\times 10^{11}$ $part/\mathrm{m}^3$).

explanation and allows us to further understand the problem to set some reasonable criteria to estimate particle density distributions. Despite the 2-D limitation of the photographs, we think that this approach can be useful to find such criteria.

The study on the preliminary design can be seen in Fig. 11 where the calculation sequence is shown. All images have been calibrated, and the external circle represents plasma chamber radius $R$, which is grounded. Fig. 11(a) shows an ultrafast picture obtained in the steady-state plasma condition, and Fig. 11(b) shows the map of plasma potential by solving (9) with the previous picture as an input with boundary conditions $\phi(R) = 0$ V and $\phi(0) = 53$ V. This value of plasma potential $V_p = 53$ V was obtained by Langmuir's probe measurements in the axis of the plasma chamber. Fig. 11(c) shows the map of self-induced electric field calculated from the plasma potential distribution by $E = -\nabla(\phi)$, and Fig. 11(d) shows the unbalanced charge distribution values $(n_i - n_e)$ expressed in particles by cubic meters that shows typical values between 1 and $4 \times 10^{16}$ $\mathrm{m}^{-3}$ regarding the color intensity scale. Moreover, as can be seen in Fig. 9, the typical electron density obtained by Langmuir's probe in the preliminary design is between 1 and $2 \times 10^{16}$ $\mathrm{m}^{-3}$. Considering a typical $\lambda_D \approx 0.1$ mm for this kind of plasma at quasi-neutrality condition, the actual length scale for the present case of quasi-neutrality breaking is estimated in 300 $\lambda_D \approx 30$ mm in a good agreement with dimensions of the observed plasma structure (plasma chamber diameter is 85 mm).

Fig. 12 shows the sequence of calculations for the optimized design with the same considerations than in Fig. 11 with the exception of plasma potential value used as a boundary condition to solve (9), where $\phi(0) = 50$ V using the plasma potential $V_p = 50$ V from Langmuir's probe measurements in the axis of the plasma chamber.

Comparison between Figs. 11 and 12 reveals interesting differences. The preliminary design presents a more expanded distribution with lower density values. This distribution was named galaxy, and it was never reported before because all our previous studies on plasma modes were made on the optimized design. As it was previously mentioned, the operational set point of the preliminary design is practically unique, and consequently, its corresponding distribution is original.

In contrast, the optimized design shows a plasma distribution where the concentration around the axis is remarkable. Densities reach the values one order of magnitude higher than in the preliminary design with a shape corresponding to the case named slug previously reported Cortázar *et al.* [20]. It is noticeable that the actual length scale of quasi-neutrality breaking is 100 $\lambda_D \approx 10$ mm. Such decrement is coherent with the reduction of average size in spatial plasma distribution as is easily noticeable in Fig. 12.

Another interesting issue is the hole in the self-induced electric field observed in Figs. 11(c) and 12(c). Both the electric field distributions show a general tendency to a radially outward direction (vectors are not represented to simplify representations), but in the case of preliminary design, the maximum values areas are closer to the chamber wall inducing a higher drain of particles from the plasma with the increase of quasi-neutrality breaking length.

## V. Conclusion

Criteria for the MW driver system design on a 2.45-GHz plasma generator are discussed based on the 3-D stationary simulations and experimental studies of EEDFs and 2-D spatial plasma distribution diagnostics by ultrafast photography. Two different approaches for designing MW driver systems have been compared by studying our preliminary and optimized sets of the plasma chamber plus the MW coupler on the TIPS ECR hydrogen plasma reactor.

On one hand, the polymodal shape of EEDFs is observed in the optimized design, as well as it was reported previously for the preliminary one. A low-energy component centered at 5.84 eV, corresponding to electrons suffering inelastic collision within the plasma, and an intermediate component at 20 eV, which was at about 13 eV in the preliminary design, are also observed. Moreover, a remaining EEDF tail composed of two components, one at 14 eV and the other at 39 eV, is reported. A comparison between EEDFs in the preliminary and optimized designs is very favorable to the last one. For B $>$ ECR, the EEDF of the optimized design exhibits a high-energy component centered at about 30 eV, which is not observed in the preliminary design. For B $=$ ECR, power absorption by electron due to ECR heating mechanism plays a more efficient role at the optimized design. Electron density and mean electron energy measured show a strong increment about 100% for electron density and 65% for mean electron energy in favor of the optimized design.

On the other hand, the study of plasma density distribution by ultrafast picture diagnostic shows a remarkable tendency to concentrate plasma around the chamber axis in favor of the optimized design. The reduction from 30 to 10 mm of the quasi-neutrality breaking scale clearly shows this fact. Moreover, densities reach values one order of magnitude higher than in the preliminary design.

Stationary electric field 3-D simulation pattern along the entire MW excitation system has been demonstrated as a remarkable tool for obtaining the optimized design and to understand some anomalous behavior of the preliminary design. Simulations allow us to think our experiment as a complex MW system that should be considered as a unified entity, which has the resonance at excitation MW frequency but with the maximum electric field intensity centered in the plasma chamber. To fulfill such requirements, a MW coupler piece is essential, and its design results a key factor in the entire designing process. This strategy implies a tailored work for each particular system and its applications. However, this is only the first step considered as a good estimation until plasma breakdown instant because a new shift of resonance frequency is produced by the plasma after its ignition [7], [35]. This new resonance frequency shift produced by plasma may be fixed by the fine-tuning stubs (see Fig. 1) as a typical method. However, this method only works for small frequency shifts and results irrelevant if the electric field distribution is too far from the desired one.

In summary, the impact of resonance cavity design on plasma density and temperature is demonstrated for the first time by two different experimental methods. Measurements of EEDFs on the plasma chamber axis and the radial spatial plasma density distribution were used to contrast how effective the design criteria are. The data clearly show the importance of the entire MW system electric field distribution 3-D simulations as an excellent approach to an optimized plasma reactor design.

## References


[1] S. Gammino, L. Celona, G. Ciavola, F. Maimone, and D. Mascali, "Review on high current 2.45 GHz electron cyclotron resonance sources," *Rev. Sci. Instrum.*, vol. 81, no. 2, Feb. 2010, Art. no. 02B313.

[2] J. Pelletier and A. Anders, "Plasma-based ion implantation and deposition: A review of physics, technology, and applications," *IEEE Trans. Plasma Sci.*, vol. 33, no. 6, pp. 1944–1959, Dec. 2005.

[3] D. Mascali *et al.*, "Microwave technology for the boost of performances in ECR ion sources," *Czechoslovak J. Phys.*, vol. 56, no. 2, pp. B1149–B1155, Oct. 2006.

[4] F. Maimone *et al.*, "Electromagnetic study and optimization of the PM-trips ion source and the related microwave line," Instituto Nazionale de Fisica Nucleare-Laboratori Nazionali del Sud, Catania, Italy, Tech. Rep. INFN/TC-07/04, Apr. 2007.

[5] L. Celona *et al.*, "On the observations of standing waves in cylindrical cavities filled by microwave discharge and ECR plasmas," in *Proc. ECRIS*, Chicago, IL, USA, Sep. 2008, pp. 15–18.

[6] L. Celona, S. Gammino, G. Ciavola, F. Maimone, and D. Mascali, "Microwave to plasma coupling in electron cyclotron resonance and microwave ion sources (invited)," *Rev. Sci. Instrum.*, vol. 81, no. 2, Feb. 2010, Art. no. 02A333.

[7] L. Celona *et al.*, "Observations of resonant modes formation in microwave generated magnetized plasmas," *Eur. Phys. J. D*, vol. 61, no. 1, p. 107–115, Jan. 2011.

[8] C. Lyneis *et al.*, "Charaterization of the microwave coupling to the plasma chamber of the lbl ecr ion source," in *Proc. ECRIS*, Grenoble, France, pp. 162–164, Sep. 2010.

[9] R. Geller, *Electron Cyclotron Resonance Ion Sources and ECR Plasmas*. Bristol, U.K.: Institute of Physics Publishing, 1996.

[10] A. Megía-Macías, O. D. Cortázar, and A. Vizcaíno-de-Julián, "Influence of microwave driver coupling design on plasma density at testbench for ion sources plasma studies, a 2.45 GHz electron cyclotron resonance plasma reactor," *Rev. Sci. Instrum.*, vol. 85, no. 3, 2014, Art. no. 033310,

[11] O. D. Cortázar, A. Megía-Macías, and A. Vizcaíno-de-Julián, "Temperature peaking at beginning of breakdown in 2.45 GHz pulsed off-resonance electron cyclotron resonance ion source hydrogen plasma," *Rev. Sci. Instrum.*, vol. 83, no. 10, Oct. 2012, Art. no. 103302.

[12] O. D. Cortázar, A. Megía-Macías, and A. Vizcaíno-de-Julián, "Experimental study of breakdown time in a pulsed 2.45-GHz ECR hydrogen plasma reactor," *IEEE Trans. Plasma Sci.*, vol. 40, no. 12, pp. 3409–3419, Dec. 2012, doi: 10.1109/TPS.2012.2222933.

[13] O. D. Cortázar, J. Komppula, O. Tarvainen, A. Megía-Macías, A. Vizcaíno-de-Julián, and H. Koivisto, "Experimental study of hydrogen plasma breakdown in a 2.45 GHz microwave discharge," *Plasma Sour. Sci. Technol.*, vol. 22, no. 1, 2013, Art. no. 015026.

[14] (2013). *Comsol Multiphysics V4.2*. [Online]. Available: http://www.comsol.com

[15] S. Djekic *et al.*, "Preliminary design of BLISI, an off resonance microwave proton source," in *Proc. ECRIS*, Grenoble, France, 2010, pp. 1–3.

[16] J. Helszajn, *Ridge Waveguides and Passive Microwave Components*, vol. 49. Bodmin, U.K.: MPG Books, 2000.

[17] D. Meeker. (2010). *Finite Element Method Magnetics V4.2*. [Online]. Available: http://www.femm.info

[18] E. Jaynes, "Theory of microwave coupling system," Naval Res. Lab., Washington, DC, USA, CRG Rep. 84, Aug. 1945.
[19] M. P. David, *Microwave Engineering*, 4th ed. Hoboken, NJ, USA: Wiley, 2012.
[20] O. D. Cortázar, A. Megía-Macías, O. Tarvainen, A. Vizcaíno-de-Julián, and H. Koivisto, "Plasma distributions observed in a 2.45 GHz hydrogen discharge," *Plasma Sources Sci. Technol.*, vol. 23, no. 6, 2014, Art. no. 065028.
[21] J. D. Swift, "Effects of finite probe size in the determination of electron energy distribution functions," *Proc. Phys. Soc.*, vol. 79, no. 4, pp. 697–701, 1962.
[22] R. R. Arslanbekov, N. A. Khromov, and A. A. Kdryavtsev, "Probe measurements of electron energy distribution function at intermediate and high pressures and in a magnetic field," *Plasma Sources Sci. Technol.*, vol. 3, no. 4, p. 528, 1994.
[23] S. V. Ratynskaia, R. J. Armstrong, and K. Rypdal, "Probe measurements of electron energy distributions in a strongly magnetized low-pressure helium plasma," *Phys. Plasmas*, vol. 6, no. 1, pp. 350–358, 1990.
[24] T. K. Popov, P. Ivanova, M. Dimitrova, J. T. Kovačič, T. Gyergyek, and M. Čereč, "Langmuir probe measurements of the electron energy distribution function in magnetized gas discharge plasmas," *Plasma Sources Sci. Technol.*, vol. 21, no. 21, 2012, Art. no. 025004.
[25] J. L. Jauberteau and I. Jauberteau, "Electron energy distribution function in plasma determined using numerical simulations of multiple harmonic components on Langmuir probe characteristic: Efficiency of the method," *Rev. Sci. Instrum.*, vol. 78, no. 4, 2007, Art. no. 043501.
[26] J. L. Jauberteau, I. Jauberteau, O. D. Cortázar, and A. Megía-Macías, "Time evolution of the electron energy distribution function in pulsed microwave magnetoplasma in $H_2$," *Phys. Plasmas*, vol. 3, no. 3, 2016, Art. no. 033513.
[27] J. L. Jauberteau, I. Jauberteau, O. D. Cortázar, and A. Megía-Macías, "Electron energy distribution function in a pulsed 2.45GHz hydrogen magnetoplasma: Study of the decay," *AIP Adv.*, vol. 7, no. 12, 2017, Art. no. 125107.
[28] O. D. Cortázar, A. Megía-Macías, A. Vizcaíno-de-Julián, O. Tarvainen, J. Komppula, and H. Koivisto, "Ultra-fast intensified frame images from an ECR hydrogen plasma at 2.45 GHz: Some space distributions of visible and monochromatic emissions," *Rev. Sci. Instrum.*, vol. 85, no. 2, 2014, Art. no. 02A902.
[29] O. D. Cortázar and A. Megía-Macías, "Strongly eccentric rotational plasma lamina observed in a 2.45-GHz hydrogen discharge," *IEEE Trans. Plasma Sci.*, vol. 44, no. 5, pp. 734–737, May 2016.
[30] O. D. Cortázar, A. Megía-Macías, O. Tarvainen, and H. Koivisto, "Experimental evidence of E×B plasma rotation in a 2.45 GHz hydrogen discharge," *Phys. Plasmas*, vol. 22, no. 12, 2015, Art. no. 123511.
[31] A. Megía-Macías and O. D. Cortázar, "Review of spatial distribution modes in a 2.45-GHz hydrogen plasma," *IEEE Trans. Plasma Sci.*, vol. 47, no. 1, pp. 483–487, Jan. 2019.
[32] O. D. Cortázar and A. Megía-Macías, "Bimodal ion energy distribution functions in a hydrogen magnetized plasma," *Plasma Sources Sci. Technol.*, vol. 28, no. 2, 2019, Art. no. 025010.
[33] H. R. Griem, *Principles of Plasma Spectroscopy*. New York, NY, USA: Cambridge Univ. Press, 1997, ch. 9, pp. 248–250.
[34] E. Bluem, S. Bechu, C. Boisse-Laporte, P. Leprince, and J. Marec, "Spatial investigation of a large diameter microwave plasma," *J. Phys. D, Appl. Phys.*, vol. 28, no. 7, pp. 1529–1533, 1995.
[35] F. Consoli, S. Barbarino, L. Celona, G. Ciavola, S. Gammino, and D. Mascali, "Investigation about the modes in the cylindrical cavity of an ECR ion source," in *Proc. PIBHI PPLA*, vol. 160. London, U.K.: Taylor & Francis, Jun. 2006, p. 467.

**Ana Megía-Macías** was born in Alcázar de San Juan, Spain, in 1985. She received the degree in mechanical engineering and the Ph.D. degree from the University of Castilla-La Mancha (UCLM), Ciudad Real, Spain, in 2008 and 2014, respectively.

In 2009, she was a Research Assistant with Sheffield Forgemaster Ltd., Sheffield, U.K. She was a Researcher with ESS Bilbao, Bilbao, Spain, from 2010 to 2016. She was a Project Associate with CERN, Geneva, Switzerland, from 2015 to 2016. She is currently an Assistant Professor with the University of Deusto, Bilbao. Her research interests include ECR ion sources, ECR plasmas, and plasma diagnostics.

**Elena Barrios-Díaz** was born in Huelva, Spain, in 1987. She received the B.Eng. degree in industrial engineering, the M.Eng. degree in nuclear instumentation, and the M.Eng. degree in industrial engineering from the University of Huelva, Huelva, in 2009, 2011 and 2015, respectively. She is currently pursuing the Ph.D. degree in plasma sources and diagnostics with the University of Castilla-La Mancha, Ciudad Real, Spain.

She was a Mechanical Engineer at CERN, Geneva, Switzerland, from 2015 to 2017. Her research interests include ECR ion sources, ECR plasmas, and plasma diagnostics.

**Jean-Louis Jauberteau** was born in Libourne, France, in 1960. He received the degree and the Ph.D. degree from the Université de Limoges, Limoges, France, in 1985 and 1988, respectively.

He held a postdoctoral position at the Technical University of Eindhoven, Eindhoven, The Netherlands, from 1988 to 1989. He is currently a Researcher with the IRCER Laboratory, CEC, Université de Limoges. His research interests include plasma chemistry and plasma diagnostics.

**Isabelle Jauberteau** was born in Paris (6eme), France, in 1960. She received the degree and the Ph.D. degree from the Université Pierre et Marie Curie, Paris, in 1984 and 1987, respectively.

She held a postdoctoral position at ETH Zürich, Zürich, Switzerland, and at the Institut de Physique, Fribourg, Switzerland, from 1988 to 1990. She was a CNRS Researcher with the Université de Villetaneuse, Villetaneuse, France, from 1990 to 1993. She is currently a Researcher with the IRCER Laboratory, CEC, Université de Limoges, Limoges, France. Her research interests include microwave (MW) plasma processes, thin metal film treatments, and plasma diagnostics.

**Osvaldo Daniel Cortázar** was born in Rosario, Argentina, in 1960. He received the degree from the National University of Buenos Aires Province Center, Tandil, Argentina, in 1986, and the Ph.D. degree in plasma physics from the National University of Mar del Plata, Mar del Plata, Argentina, in 1990.

He held a postdoctoral position at Colorado State University, Fort Collins, CO, USA, from 1990 to 1994 (X-ray lasers capillary discharges). He is currently the Head of the Ion Sources Laboratory and an Associate Professor at the University of Castilla-La Mancha, Ciudad Real, Spain. His research interests include ECR plasma sources, plasma diagnostics, and pulsed power technology.